PNAS RESEARCH ARTICLE | ENGINEERING

Chelation-directed interface engineering of in-place self-cleaning membranes

Xiaobin Yang[a], Yangxue Li[a], Dan Wu[b], Linlin Yan[c], Jingzhu Guan[a], Yajie Wen[a], Yongping Bai[a], Bhekie B. Mamba[d], Seth B. Darling[e,f,g,1], and Lu Shao[a,1]

Edited by Alexis Bell, University of California, Berkeley, CA; received November 5, 2023; accepted January 31, 2024

Water–energy sustainability will depend upon the rapid development of advanced pressure-driven separation membranes. Although energy-efficient, water-treatment membranes are constrained by ubiquitous fouling, which may be alleviated by engineering self-cleaning membrane interfaces. In this study, a metal-polyphenol network was designed to direct the armorization of catalytic nanofilms (ca. 18 nm) on inert polymeric membranes. The chelation-directed mineralized coating exhibits high polarity, superhydrophilicity, and ultralow adhesion to crude oil, enabling cyclable crude oil-in-water emulsion separation. The in-place flux recovery rate exceeded 99.9%, alleviating the need for traditional ex situ cleaning. The chelation-directed nanoarmored membrane exhibited 48-fold and 6.8-fold figures of merit for in-place self-cleaning regeneration compared to the control membrane and simple hydraulic cleaning, respectively. Precursor interaction mechanisms were identified by density functional theory calculations. Chelation-directed armorization offers promise for sustainable applications in catalysis, biomedicine, environmental remediation, and beyond.

membrane | water treatment | chelation | catalytic self-cleaning | oil separation

Significance

Pressure-driven membrane separation promises low-carbon water treatment toward a sustainable energy–water nexus. However, conventional membrane processes are severely constrained by ubiquitous fouling and accompanying energy- and cost-intensive cleaning. Advanced self-cleaning antifouling membranes would represent a breakthrough in this sector. Herein, a chelation-directed interface mineralization strategy is reported for fabricating highly polarized superhydrophilic ultrathin coatings on inert polymeric membranes by aqueous dip-coating at room temperature. The mineralized membrane could realize in-place catalytic self-cleaning for highly efficient membrane regeneration. This simple, mild, and green method alleviates the need for the traditional removal of membrane modules from operation thereby circumventing significant economic and productivity costs. This method also offers promise for sustainable applications in catalysis, biomedicine, environmental remediation, and beyond.

Currently, at least two billion people cannot access safe drinking water, and nearly half of the population will be living in severely water-stressed areas by 2050 (1). Supplementing supplies of fit-for-purpose clean water by wastewater treatment will be increasingly crucial for water sustainability (2–5). Therein, membrane-based technologies have been widely exploited owing to their high separation efficiency and ease of scaling up (6–9). However, various solutes and suspended species (oil, proteins, etc.) easily adsorb on the membrane interfaces, particularly for hydrophobic polymeric membranes, due to electrostatic and hydrophobic interactions (3, 10–12). Aggressive fouling deteriorates membrane permselectivity and necessitates frequent energy-/cost-intensive hydraulic/chemical cleaning (13–17). The passive antifouling capacity of a material is closely tied to the molecular structure and polarity (18). Active antifouling capacity is typically achieved using catalytic reactivity (14, 19). Engineering highly polarized catalytic self-cleaning nanofilms at the membrane interface to integrate active catalytic foulant degradation, complementing conventional passive hydration antifouling, into the water treatment process is a compelling strategy (14, 20–22). Most fabrication methods necessitate heating, strong oxidants, or strong acid. Moreover, such films generally compromise membrane permeability due to pore shrinkage derived from large thicknesses. Constructing self-cleaning films on inert polymeric membranes under mild conditions remains challenging. A potential route to overcome this challenge is controllable and mild hydrolysis of mineral precursors to prepare an ultrathin catalytic oxide mineral film.

With this in mind, the chelation interaction between metal ions and polyphenols is a good candidate, capable of forming an ultrathin metal-polyphenol network (MPN) (23, 24). Meanwhile, MPNs possess effective interface adhesion for immobilization on inert material surfaces (25–28). MPNs could also provide abundant nucleation sites for mineral immobilization and growth (24, 29). Thus, MPNs were adopted as an intermediate layer to direct subsequent conformal mineralization of catalytic oxide within porous membranes at ambient temperature.

Herein, hydrophobic polyvinylidene fluoride (PVDF) membranes are engineered by aqueous mineralization engineering (mineral precursor, $MnSO_4$) directed by an intermediate MPN layer [assembly of $MnSO_4$ and tannic acid (TA)]. The procedure involves dip-coating in alkaline aqueous buffers (pH = 8.5) under ambient conditions (Fig. 1). The as-prepared highly polarized superhydrophilic mineralized membranes are used for minimizing fouling and in-place catalytic self-cleaning during crude oil-in-water emulsion separation. The chemical composition, structure/morphology, wettability, and mechanical properties are investigated experimentally, and the chelation-directed mineralization mechanism is unveiled using density functional theory (DFT) calculations. Figures of merit of catalytic self-cleaning and hydraulic cleaning and membrane stability are established and

The authors declare no competing interest.

This article is a PNAS Direct Submission.

[1]To whom correspondence may be addressed. Email: darling@anl.gov or shaolu@hit.edu.cn.

This article contains supporting information online at https://www.pnas.org/lookup/suppl/doi:10.1073/pnas.2319390121/-/DCSupplemental.

Published March 4, 2024.

contrasted. This study provides a route for the eco-friendly construction of active catalytic self-cleaning membranes for energy-efficient water treatment.

Results

Membrane Morphology and Structure. Membrane structure and morphology were investigated to characterize the directed mineralization of MnO_2 nanoarmor on the hydrophobic membrane (Fig. 2). With regard to SEM images (Fig. 2 *A*–*F*, for reduced magnification see *SI Appendix*, Fig. S1), coating with MPN (M-MPN) by itself resulted in a negligible change in morphology compared to the nascent membrane (M-Nascent); material surfaces are smooth, indicating a uniform deposition. Incubation of the Mn^{2+} precursor (M-M) without MPN resulted in sparse and scattered particles. In contrast, the MPN-mediated mineralized membrane M-MPN-M exhibited dense nanoparticles. According to the Wenzel model (30), rough nanoprotrusions could increase hydrophilicity. In addition, energy-dispersive X-ray spectroscopy (EDS) mapping was performed on the cross-section of M-MPN-M to detect the element distribution. The elements representative of the coating exhibited a uniform distribution across the detection region (Fig. 2 *G* and *H* and *SI Appendix*, Fig. S2), indicating that the mineral film at the membrane interface is conformal and uniform. M-MPN-M was further measured by transmission electron microscopy (TEM) to analyze the detailed structure of the mineralized film. The film generated at the membrane surface is crystalline. Its lattice spacing is 0.69 nm, belonging to the (0,0,1) face of δ-MnO_2. These results indicate that the chelation effect could effectively enable ambient-temperature aqueous ordered mineralization of MnO_2 rather than amorphous hydrolysis (the reaction equation displayed in *SI Appendix*, Fig. S3). This method of mild mineralization of crystalline nanofilms offers promise for various applications of such functional materials.

Chelation-Directed Mineralization Mechanism

The crystalline MnO_2 nanofilm was nucleated and grown on the intermediate MPN layer. Elucidating possible molecular interaction mechanisms of TA and Mn^{2+} is crucial to interpreting the MPN formation and subsequent directed mineral nucleation. DFT calculations were performed in an aqueous system. TA was simplified to a gallate branch for computational efficiency. Phenolic hydroxyl and ester moieties are expected to yield strong interactions with Mn^{2+} (Fig. 3*A*). The former results in a binding energy of −2.04 eV with an O-Mn bond with a distance of 2.12 Å (Fig. 3*b*1). The latter exhibits a binding energy is −1.49 eV at an O-Mn bond with a relatively short distance of 1.97 Å (Fig. 3*c*1); the Mn atom is ortho to the carbonyl oxygen. Relatively, the phenolic hydroxyl moieties have higher binding energy with Mn^{2+} than the ester moiety, possibly due to the collective chelation of two adjacent hydroxyl groups and indicating a dominant role. Their electron cloud distributions also indicate substantial integration and strong interactions (Fig. 3 *b*2 and *c*2).

To quantify the electron density differences brought by precursor interactions, multifunctional wavefunctions were further analyzed in terms of 3D isosurfaces and 2D contour maps (Fig. 3 *D* and *E*). The gallate–Mn interactions resulted in blue electron-rich bell-like structures surrounding the yellow electron-deficient Mn cores (Fig. 3 *d*1 and *e*1, other scenes see *SI Appendix*, Figs. S4 and S5). The phenolic hydroxyl moieties exhibit two electron-deficient arms surrounding the above shell. The ester moiety displays one arm tethered to the shell. From the 2D contour maps (Fig. 3 *d*2 and *e*2), the O–M intermediate interaction areas indicate sharply increased electron density around Mn^{2+}, relative to the clear decrease in the gallate branch. All the results indicate that TA and Mn^{2+} could generate electron integration and interactions, collectively contributing to MPN deposition and subsequent ordered mineral nucleation and crystalline growth.

Physicochemical Characterization

The physicochemical properties of the as-prepared membranes were further studied. First, wettability was characterized by initial (Fig. 4*A*) and dynamic (*SI Appendix*, Fig. S6) water contact angles (WCAs). The nascent membrane is hydrophobic with a WCA of 119.5°. The TA/Mn^{2+}-coated M-MPN membrane became more hydrophilic with an initial WCA of 41.2°. Similarly, the Mn^{2+}

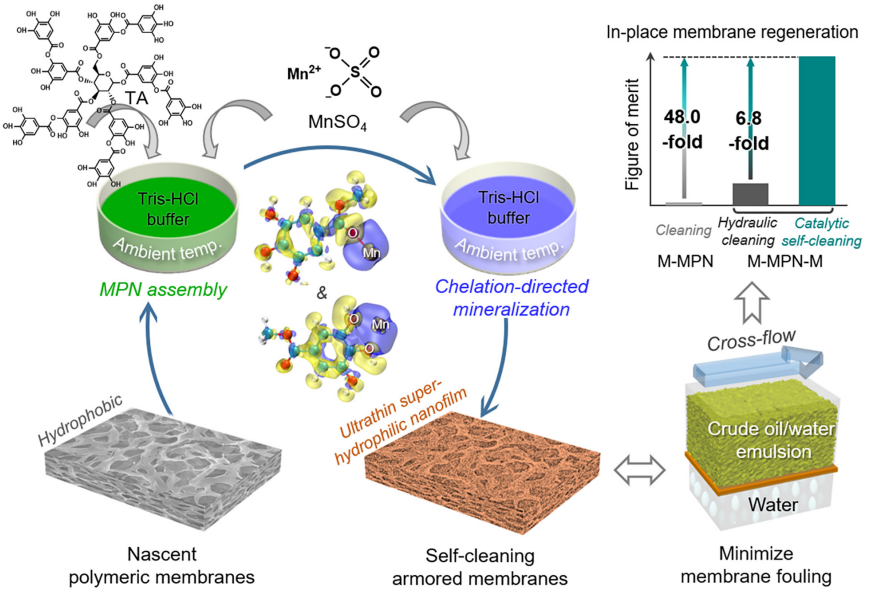

Fig. 1. Scheme of ambient-temperature chelation-directed mineralization engineering of a self-cleaning membrane. The hydrophobic polymeric membrane is first dip-coated in an alkaline aqueous buffer containing TA and $MnSO_4$. Then, the MPN directs δ-MnO_2 mineralization at the membrane interface in $MnSO_4$ solution via chelation interactions. The resultant highly polarized membrane is used to minimize fouling and realize in-place self-cleaning during repeated crude oil–water emulsion separations. The regeneration efficiency of catalytic self-cleaning is superior to that of hydraulic cleaning.

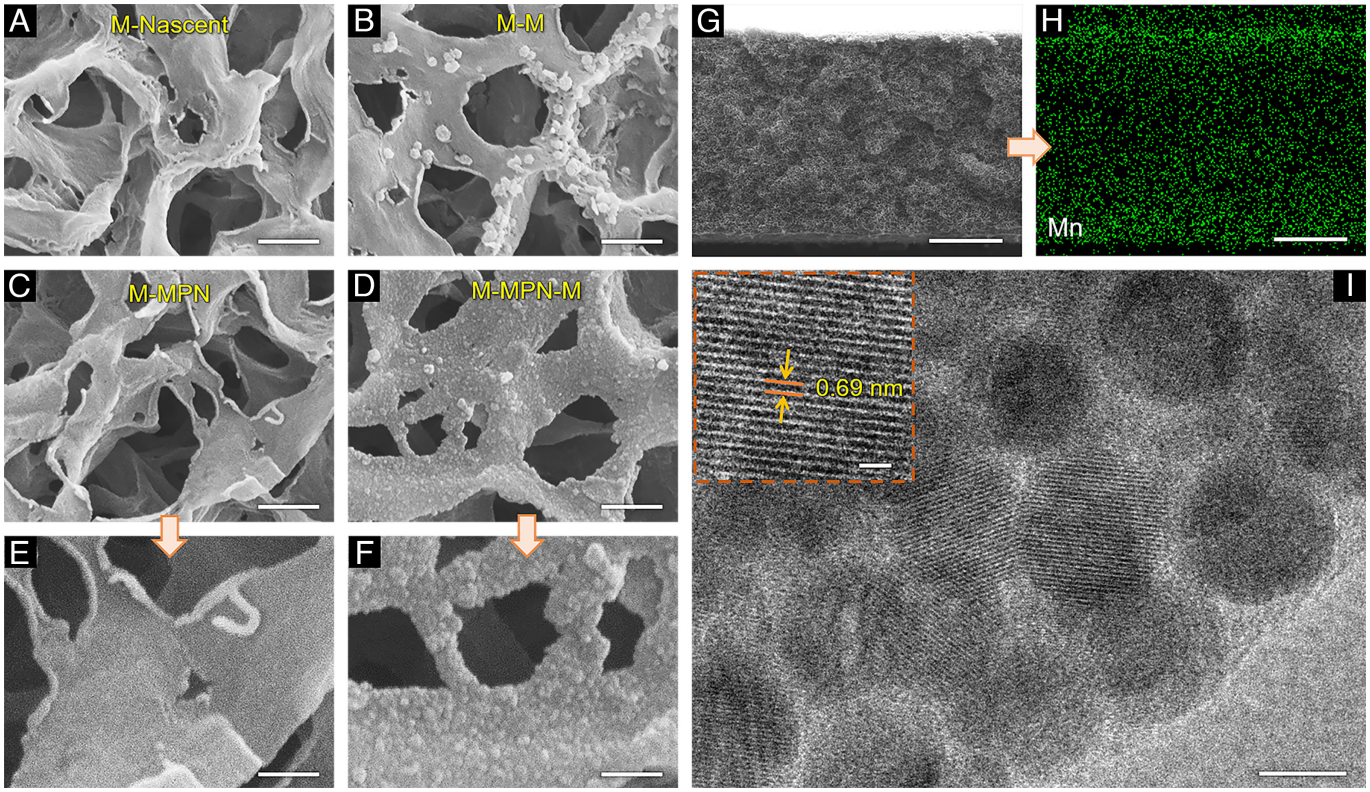

Fig. 2. Membrane structure and morphology. (*A–F*) SEM images of the surfaces of (*A*) M-Nascent, (*B*) M-M, (*C* and *E*) M-MPN, and (*D* and *F*) M-MPN-M. (*G*) Cross-section SEM image of M-MPN-M and (*H*) EDS mapping of Mn. (*I*) TEM image of M-MPN-M, the *Inset* is a magnified view. Scale bars in (*A–D*) are 500 nm, in (*E* and *F*) are 200 nm, in (*G* and *H*) are 40 μm, in (*I*) are 10 nm, and in the *Inset* of (*I*) are 2 nm.

dip-coated control membrane M-M exhibited moderate hydrophilization with an initial WCA of 85.2°. In stark contrast, the MPN-mediated mineralized membrane M-MPN-M was superhydrophilic (0°); the red circle shows the water droplet pulled apart (water instantly penetrated through the membrane cross-section). In combination with ethylene glycol contact angles (*SI Appendix*, Fig. S7), apparent surface energies of membranes were deduced as well as polar compositions (often contributive to hydration capability). As shown in Fig. 4*A*, M-MPN-M exhibits the highest values: total surface energy of 90.3 mN m^{-1} (2.6-fold to M-Nascent, 1.6-fold to M-MPN) and polar composition of 88.9 mN m^{-1} (64.4-fold to M-Nascent, 1.9-fold to M-MPN). The highly polarized and superhydrophilic mineralized membrane implies a strong hydration capability preventing foulants from approaching the membrane interface during water treatment.

Next, ATR-FTIR (Fig. 4*B*) and XPS (Fig. 4 *C–E*) measurements were performed to characterize the surface chemistry. With regard to ATR-FTIR in Fig. 4*B*, M-MPN showed new peaks at 1,725 cm^{-1} for the stretching mode of carbonyl groups from TA and 1,600 cm^{-1} for the stretching mode of C=C bonds from the aromatic ring (this peak shifted to 1,575 cm^{-1} for M-MPN-M possibly due to the metal bound effect) compared to M-Nascent. M-MPN-M exhibited a significant increase in peak intensity at 3,100 to 3,600 cm^{-1} for -OH stretching derived from aqueous mineralization and new peaks originating from MnO_2 arose at 500 to 590 cm^{-1} (stretching vibration) and at 620 to 720 cm^{-1} (wagging vibration), indicating the generation of a manganese oxide coating. For XPS (Fig. 4*C*), M-M only produced a small Mn peak (0.63 At.%) owing to the lack of sufficient nucleation sites. M-MPN exhibited a 3.1-fold rise in O content as compared to M-Nascent, indicating a large increase in reactive sites. M-MPN-M showed strong peaks of Mn (25.5-fold to M-M) and O, and the F peak decreased sharply (95.3% to M-Nascent). Furthermore, peaks of O 1s and Mn 2p were fitted to explore the nature of the molecular bonding. For O 1s (Fig. 4*D*), it integrates MnO_2 (529.7 eV), -OH (530.9 eV) derived from the aqueous mineralization process and from phenolic hydroxyl groups, and C=O (531.3 eV) and C-O (532.4 eV) from TA. Mn 2p (Fig. 4*E*) contains two isolated peaks of Mn $2p_{1/2}$ and Mn $2p_{3/2}$; both peaks include Mn^{3+} (641.5 eV and 653.1 eV) and Mn^{4+} (644.0 eV and 656.5 eV). The abundant Mn^{3+} indicates plentiful oxygen vacancies in the mineralized MnO_2, which is beneficial for providing reactive oxygen species (ROS) during catalysis. MPN formation was also verified by differences in UV–vis spectra and precipitation of the incubated aqueous solutions (*SI Appendix*, Fig. S8).

The pore size distributions of the as-prepared membranes were measured to deduce the coating thickness (Fig. 4*F*). The thickness was determined in terms of half of the pore diameter reduction value when referring to the control membrane (*SI Appendix*, Fig. S9). The thicknesses of the MPN film and MPN-M film are deduced to be about 6 nm and 18 nm, respectively. The bottom interface of the MnO_2 mineral film may be intermixed within the MPN intermediate film. The ultrathin nature of the coating minimizes the negative influence of pore reduction on permeability.

To evaluate oil repellency, underwater crude oil adhesion forces of the as-prepared membranes were measured (Fig. 4 *G* and *H*). M-MPN-M exhibits a minimal crude oil adhesion force of 0.7 μN, a 97.6% decrease relative to M-MPN. This is ascribed to the collective influence of superhydrophilicity, high surface energy, and strong polarity of the mineralized nanofilm. Crude oil adhesion forces of other membranes were also measured for contrast. The crude oil adhesion force of M-MPN-M decreased by over 98% compared to other membranes; 99.0% for M-Nascent and 98.8% for M-M. Furthermore, underwater crude oil contact angles were measured and oil adhesion works were deduced

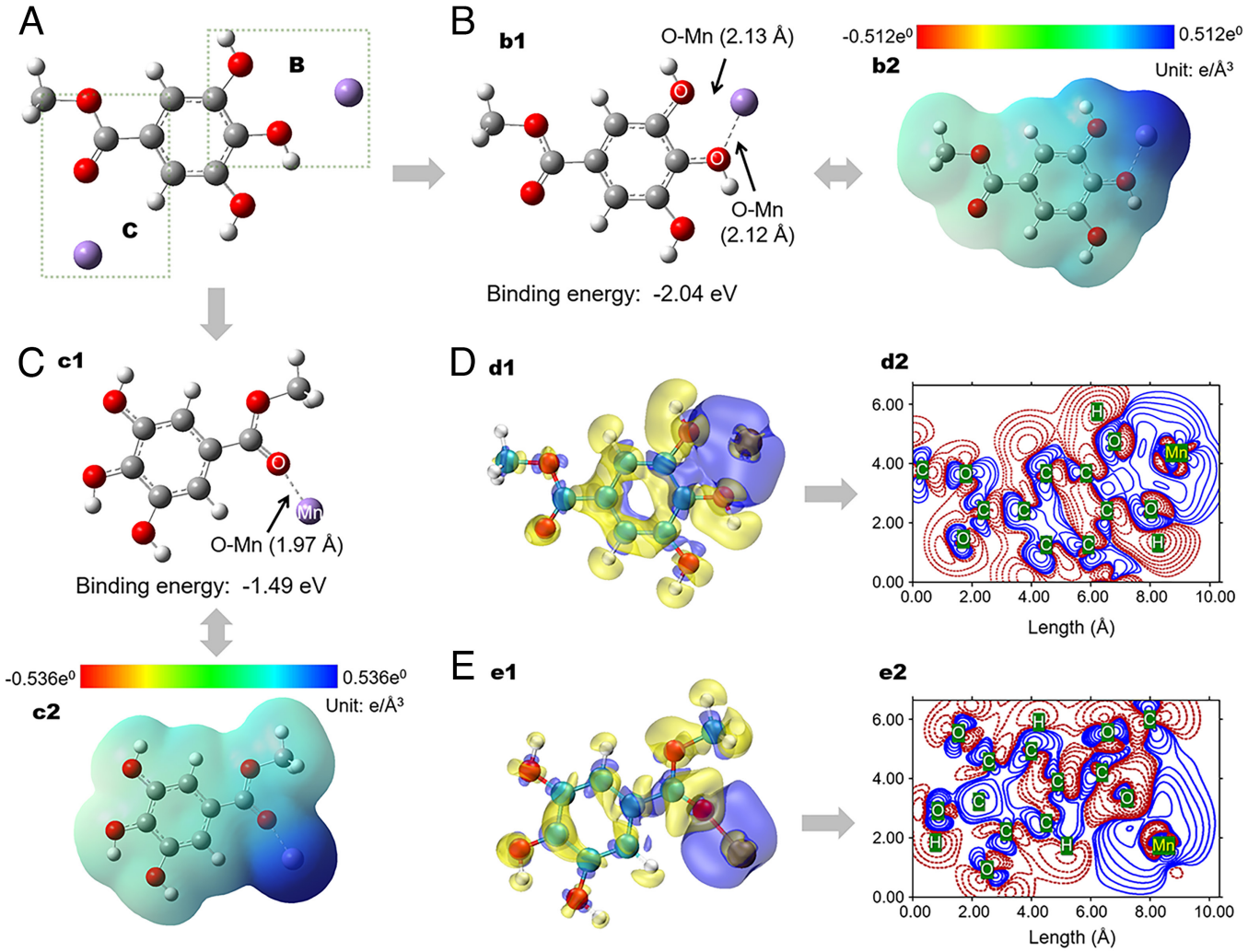

Fig. 3. Computational modeling. (*A*–*C*) DFT calculations. (*A*) Two configurations of a system with one gallate branch from the TA molecule and one Mn^{2+}. (*B* and *C*) Equilibrium states of the system originating from interactions with (*b*1) phenolic hydroxyl and (*c*1) ester groups. (*b*2 and *c*2) Corresponding electron cloud spatial arrangement. (*D* and *E*) Electron density difference analysis of the equilibrium states. The 3D isosurfaces and corresponding 2D contour maps of the electron density difference (*d*1 and *d*2) located beside hydroxyl groups and (*e*1 and *e*2) beside the ester group, respectively. The blue and yellow surfaces in the 3D isosurfaces represent isovalues of 0.0006 and –0.0006, respectively. The blue solid lines and red dashed lines in the 2D contour maps correspond to the regions with increased/decreased electron density, respectively.

(Fig. 4*I*). M-MPN-M is underwater superoleophobic with a crude oil contact angle of 170.2°. The work of adhesion indicates the adhesion strength of oil on the membrane surface underwater (31). M-MPN-M exhibits a minimal crude oil adhesion force of 0.8 mJ m^{-2}, indicating a 98.5% and 93.4% decrease relative to M-Nascent and M-MPN, respectively. The ultralow crude oil adhesion of M-MPN-M enables its significant potential for efficient crude oil-in-water emulsion treatment.

Membrane Separation Performance

A superhydrophilic interface is generally beneficial for mitigating membrane fouling during water treatment. Thus, the superhydrophilic MnO_2-mineralized membrane M-MPN-M was examined for its antifouling capacity toward crude oil-water emulsion separations. First, pure water fluxes were measured via a cross-flow filtration apparatus (Fig. 5*A*). All modified membranes exhibited some improvement compared to the nascent membrane due to their differences in polarity, wettability, and compression resistance; M-MPN-M presented the highest water permeance of 7917 L m^{-2} h^{-1} bar^{-1}, a 58.3% increase compared to M-Nascent (*SI Appendix*, Fig. S10). The large increase in permeance is ascribed to the enhanced hydrophilicity and the more compression-tolerant rigid coating. Furthermore, water permeances of dry membranes were compared to reveal hydration capability differences and potential for dry-state storage; M-MPN-M has the highest permeance-retaining ratio of 99.0% relative to the wet one (*SI Appendix*, Fig. S11). The pressure–flux relationship was investigated for M-MPN-M, exhibiting relatively consistent pressure-normalized permeance (*SI Appendix*, Fig. S12); water permeance under 0.3 bar retains 98.9% of that under 1.0 bar (*SI Appendix*, Fig. S13). Thus, for ease of operation, a low operating pressure of 0.3 bar was used to perform repeated crude oil-in-water emulsion separations using M-MPN-M and M-MPN. M-MPN-M began with a permeance of 6,436 L m^{-2} h^{-1} bar^{-1} and gradually decreased over time to 2,806 L m^{-2} h^{-1} bar^{-1} after 30 min of filtration (Fig. 5*B*). Critically, the mineralized membrane could regenerate substantially with pure water permeation (*SI Appendix*, Fig. S14), and emulsion permeance was nearly fully recovered via in-place cleaning by an H_2O_2 aqueous solution. The oil rejection ratios surpassed 99.9% with a resultant TOC value of 9.7 ppm (optical images of feed and filtrate solutions in *SI Appendix*, Fig. S15, TOC and oil rejection ratio in *SI Appendix*, Fig. S16). In contrast, M-MPN began with a permeance of 3,291 L m^{-2} h^{-1} bar^{-1} and

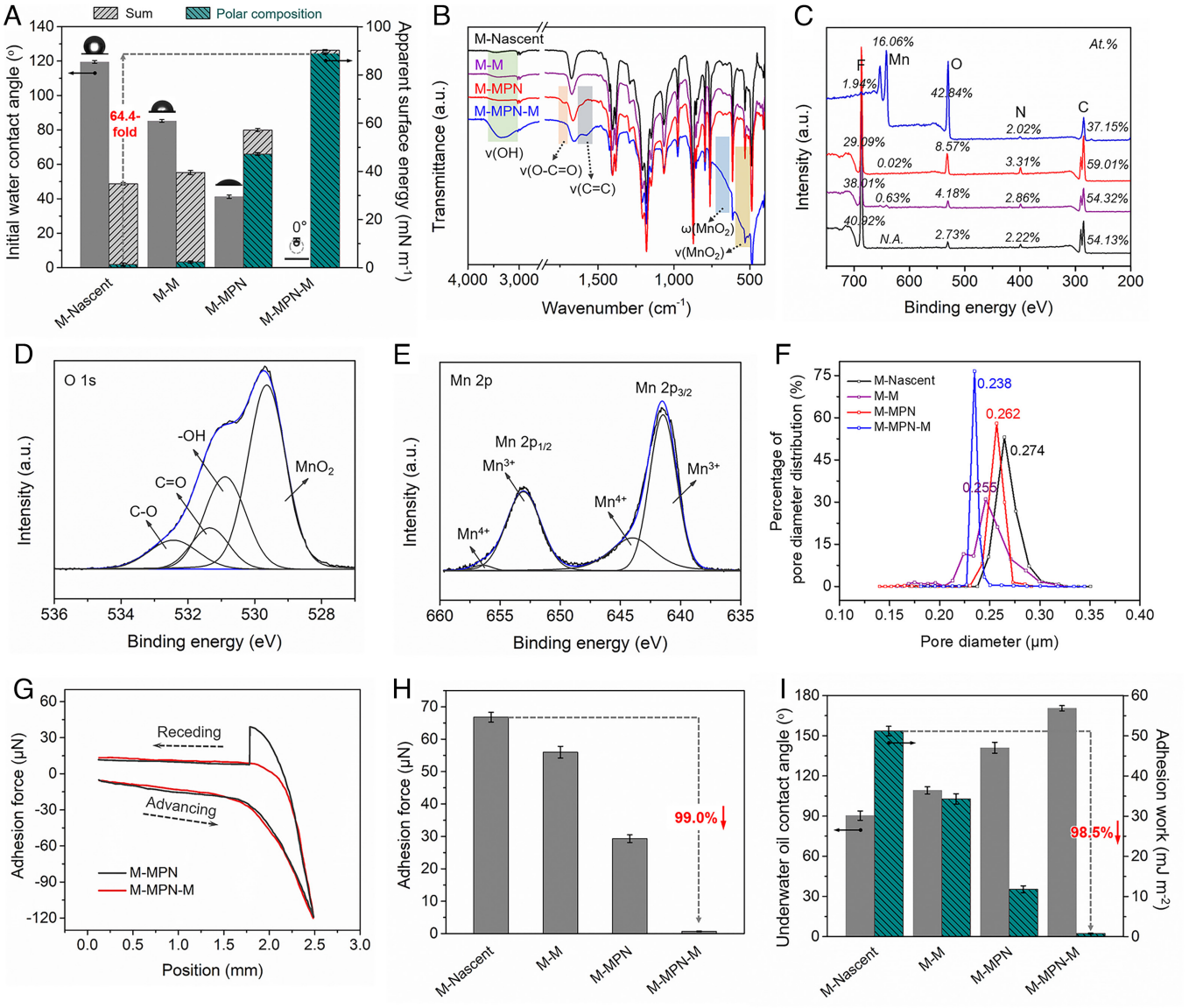

Fig. 4. Physicochemical characterization of as-prepared membranes. (*A*) Initial WCAs and apparent surface energy. The *Insets* are water droplet shapes. (*B*) FTIR spectra. (*C*) X-ray photoelectron spectroscopy (XPS) spectra, the line colors correspond to the colored codes in (*B*). (*D*) O 1s and (*E*) Mn 2p peak fitting of M-MPN-M. (*F*) Pore size distribution. (*G*) Underwater adhesion force curve of crude oil on M-MPN and M-MPN-M. (*H*) Underwater crude oil adhesion force. (*I*) Underwater crude oil contact angles and oil adhesion work on the membrane surface.

sharply decreased to 495 L m^{-2} h^{-1} bar^{-1}. The pure water and emulsion permeances could not be recovered by a similar in-place H_2O_2 cleaning. In addition, the in-place cleaning efficacies of M-MPN-M by water and H_2O_2 solution were compared by recording their real-time permeance recovery after one-cycle emulsion separation (Fig. 5*C*). Their permeance recovery data were fitted by a continuous exponential growth model using Eq. **1**:

$$J = a\left(1 - e^{\frac{-t}{b}}\right) + J_0, \qquad [1]$$

where a indicates the maximum permeance recovery amplitude, b indicates a characteristic recovery time, J_0 is the initial normalized flux, and t is the rinsing time. The water permeance regenerated by water (hydraulic cleaning) and H_2O_2 solution (catalytic self-cleaning) follows Eqs. **2** and **3**, respectively:

$$J_{hc} = 0.40\left(1 - e^{\frac{-t}{4.14}}\right) + 0.36, \qquad [2]$$

$$J_{csc} = 0.61\left(1 - e^{\frac{-t}{0.93}}\right) + 0.36. \qquad [3]$$

Given the values of a (0.61 to 0.40), the catalytic self-cleaned membrane has an in-place 1.5-fold higher permeance recovery amplitude than the hydraulic-cleaned membrane. The former could recover the water permeance beyond 99.9% (measured by pure water, the real-time recovered permeance is 97.0% due to generated bubbles in the permeate pipe), whereas the latter reached 72.3%. The catalytic self-cleaned membrane featured a characteristic recovery time of 0.93 min, which is faster than that of the water-cleaned membrane of 4.14 min.

In addition, the figure of merit of a/b was defined to better evaluate the in-place regeneration efficiency. The membrane exhibits a 6.8-fold higher figure of merit of regeneration by in-place catalytic self-cleaning compared to hydraulic cleaning; $\frac{a_{csc} \times b_{hc}}{a_{hc} \times b_{csc}} = 6.8$. During the catalytic cleaning process, the MPN-mediated MnO_2-mineralized coating could catalyze the

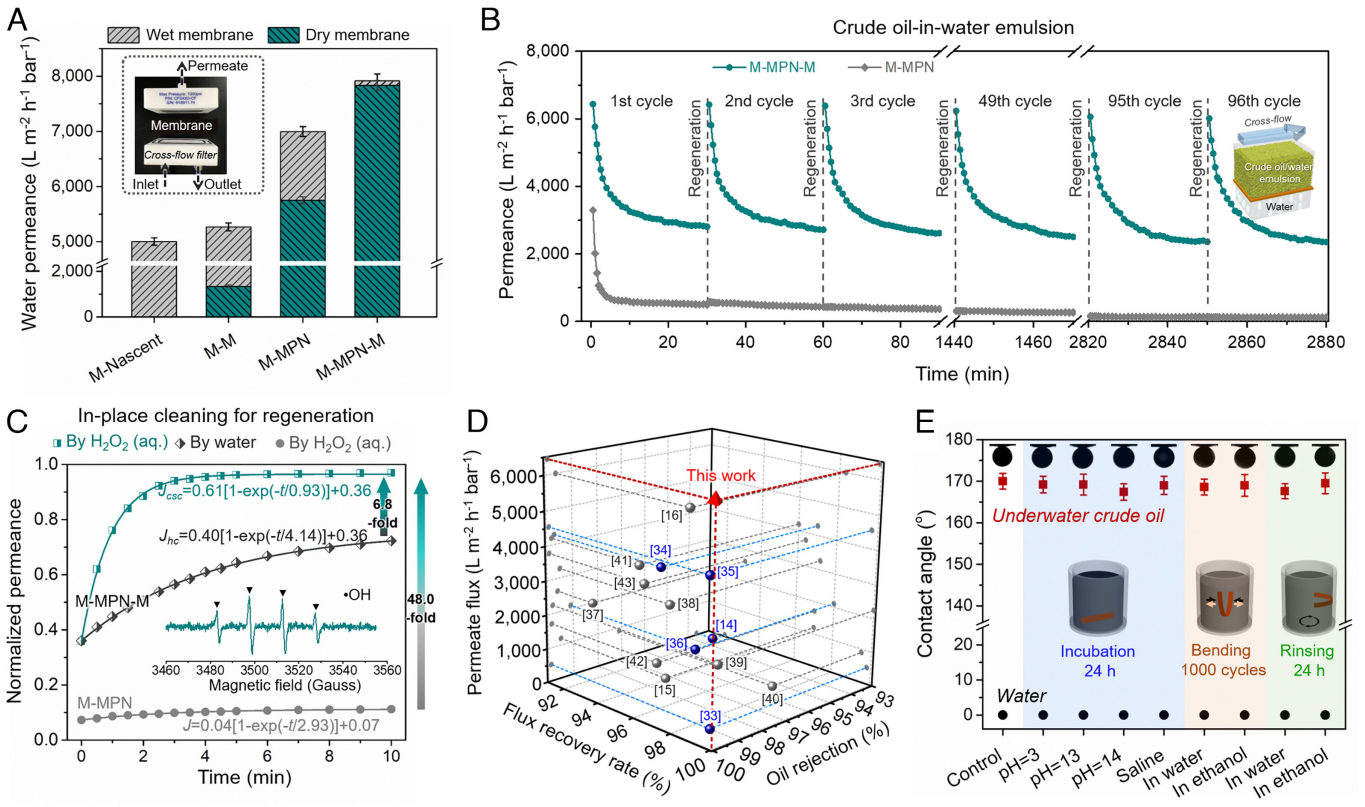

Fig. 5. Membrane cross-flow separation performance and stability evaluation. (*A*) Water permeances of wet/dry membranes. The *Inset* is a cross-flow filter. (*B*) Permeance-time functions of M-MPN-M and M-MPN during in-place crude oil-in-water emulsion separation assays. (*C*) Membrane regeneration performance of M-MPN-M by in-place H_2O_2 cleaning or water cleaning and of M-MPN by in-place water cleaning after one-cycle separation. The *Inset* is ROS detected by EPR in a H_2O_2 solution. (*D*) Performance comparison with state-of-the-art membranes. The blue data are membranes with catalytic functions. (*E*) Membrane stability evaluation of M-MPN-M after various treatments in terms of water/underwater oil contact angles.

decomposition of H_2O_2 to produce O_2 bubbles from the interface between the cake layer and the membrane skeleton surface. The in-place generated bubbles (*SI Appendix*, Fig. S17) can quickly remove the accumulated cake layer through physical force. Early-stage regeneration (before the characteristic recovery time) is dominated by this process. Furthermore, bubbles can spontaneously coalesce with oil droplets due to their similar surface tension and carry them away from the membrane surface by increasing their buoyancy (32). Moreover, ROS were detected in dilute H_2O_2 solution by an electron paramagnetic resonance (EPR) spectrometer (*Inset* in Fig. 5*C*). These ROS could degrade the residual organic foulants such as oil and surfactant left on the membrane surface and pores. Therefore, apart from hydration-induced passive antifouling, the improvement in the recovery rate (in terms of the characteristic recovery time) and the resulting flux recovery ratio are collectively attributed to the aforementioned two factors (O_2 bubbles to repel and ROS to degrade) (*SI Appendix*, Fig. S18). In addition, the water permeance of M-MPN regenerated by H_2O_2 solution is fitted by Eq. **4**.

$$J = 0.04(1 - e^{\frac{-t}{2.93}}) + 0.07. \quad [4]$$

M-MPN-M exhibits a 48.0-fold figure of merit for in-place catalytic self-cleaning compared to M-MPN. The irreversible oil fouling of M-MPN was ascribed to its nonideal hydration protective layer derived from inadequate hydrophilicity. In comparison to many state-of-the-art membranes (Fig. 5*D*) (14–16, 33–43), our mineralized catalytic membrane M-MPN-M exhibits its superior permeance, oil rejection, and permeance recovery ratio.

Membrane Stability Evaluation

Membrane stability in separation applications was further evaluated in various feed environments. Membrane wettability was investigated for M-MPN-M samples after incubation in acid/alkali (pH = 3, 13, 14) and saturated NaCl solution, 1,000-cycle bending in water/ethanol, and 24 h rinsing in water/ethanol. Fig. 5*E* shows the WCAs and underwater OCAs of the treated membranes. The treated membranes exhibited superhydrophilicity with WCAs of 0° and underwater superoleophobicity with crude oil contact angles beyond 160° even after these rigorous treatments. In addition, SEM images of M-MPN-M after 3-cycle regeneration did not exhibit obvious change (*SI Appendix*, Fig. S19). The results indicated that the superhydrophilic MnO_2 mineralized film at the membrane interface is remarkably stable, likely as a result of the strong interactions identified via DFT modeling described above. All the treated samples demonstrated excellent oil repellency. In addition, the water-wetting and penetration behaviors (*SI Appendix*, Fig. S20), pure water fluxes (*SI Appendix*, Fig. S21), and oil rejection ratios (*SI Appendix*, Fig. S22) of M-MPN-M membranes with various post-treatments were studied. A negligible change in performance is exhibited after these harsh treatments, suggesting that facile chelation-directed ambient-temperature mineralization holds promise for applications in practical water treatment as well as in environmental remediation.

Discussion

Mild and controllable preparation of high-performance self-cleaning membranes is promising for achieving a sustainable water–energy nexus. An MPN chelation-mediated manganese oxide mineralization was designed for fabrication of superhydrophilic catalytic

self-cleaning membranes. The highly polarized mineralized nanofilm at the membrane interface exhibits ultralow crude oil adhesion, cyclable crude oil-in-water emulsion separation, and high-efficiency in-place self-cleaning capacity. The nanoarmored membrane exhibits greatly enhanced figures of merit of in-place catalytic self-cleaning regeneration compared to the control membrane and to simple hydraulic cleaning. The self-cleaning membrane shows a flux recovery rate and oil rejection beyond 99.9%. Theoretical calculations and wavefunction analysis reveal strong precursor interaction mechanisms visualized as electron-rich bell-like structures surrounding the electron-deficient Mn cores. The mineralized membranes could withstand rigorous treatments, capable of dealing with various complex wastewater feed streams. Such mild chelation-directed mineralization strategy suggests opportunities in practical water-remediation applications and in the fields of material science, nanotechnology, catalysis, biomedicine, and beyond.

Materials and Methods

Materials. Hydrophobic PVDF microfiltration membranes (pore size of about 0.22 μm) were purchased from Membrane Solutions (USA). Tris was purchased from Sigma-Aldrich (USA). TA, $MnSO_4$, ethanol, and ethylene glycol were purchased from Aladdin (China). HCl was supplied by Tianjin Kermel (China). Crude oil was supplied by a local factory.

Membrane Preparation. Original membranes were washed with ethanol and water before modification. After initial optimization, TA (0.2 g) and $MnSO_4$ (0.05 g) were simultaneously dissolved into aqueous buffers (40 mL of 50 mM Tris-HCl). After 1 h of incubation, the membranes were washed with buffer three times. Then, the membranes were further incubated in $MnSO_4$ solution (0.2 g in 40 mL Tris-HCl buffer) for 9 h at room temperature to obtain mineralized membranes. Unitary MPN modification or $MnSO_4$ incubation (in buffer) of the nascent membrane was also performed as the control sample.

Characterization. Water/ethylene glycol/oil contact angles were measured by an SL-200 KB detector. The apparent surface energy of one membrane was collectively deduced by contact angles of water and ethylene glycol according to Eqs. **4** and **5**:

$$\gamma_l(1+\cos\theta) = 2\left(\gamma_l^p\gamma_m^p\right)^{\frac{1}{2}} + 2\left(\gamma_l^d\gamma_m^d\right)^{\frac{1}{2}}, \quad [5]$$

$$\gamma_m = \gamma_m^d + \gamma_m^p, \quad [6]$$

where γ denotes the apparent surface energy, the subscripts l and m denote the test liquid and membrane, and the superscripts d and p denote dispersive and polar components, respectively. θ denotes the measured contact angles. The underwater crude oil adhesion work on the membrane surface was deduced by Eq. **6**:

$$W = \gamma(1+\cos\theta), \quad [7]$$

where W denotes the adhesion work, γ denotes the interface tension between crude oil and water, and θ denotes underwater crude oil contact angles. Membrane chemistry was revealed by ATR-FTIR (PerkinElmer, USA) and XPS (Shimadzu AXIS Ultra DLD, Japan). Membrane mechanical properties were measured by an electronic universal analyzer (Instron 5500R, USA) when setting the sample size at 5 mm × 20 mm. The membrane pore size distribution was measured by a membrane pore size tester (BSD-PB). Membrane morphology was captured by SEM (Nanosem 430), and element distribution mapping was determined by an EDS detector. TEM images were measured using a sliced membrane nanosheet by a TEM machine (JEM-2100) with an acceleration voltage of 200 kV. ROS were measured using an EPR spectrometer (Bruker EMX-PLUS, Germany).

Emulsion Preparation and Separation Assays. Crude oil-in-water emulsions (2%, v/v) were prepared by 2 min of sonication and 3 h of stirring. Repeated membrane separation assays were performed in a cross-flow filtration device with a test area of 33.0 cm^2. The pure water flux/permeance was measured under 1.0 bar. Emulsion separation and cleaning were performed at 0.3 bar. The permeate flux was calculated by Eq. **8**.

$$J = \frac{V}{(A \times t \times \Delta P)}, \quad [8]$$

where J indicates the permeate flux (L m^{-2} h^{-1} bar^{-1}), and V, A, and t indicate the filtrate volume, membrane test area, and test time, respectively. ΔP is the test pressure (bar). During emulsion separations, pure water was allowed to permeate for about 1 h until its performance is stable, then emulsions were filtrated. Oil rejection (R) was deduced by Eq. **9** when comparing the oil concentration in the feed (C_f) and permeate (C_p) solutions using a TOC detector (multi N/C 3100, Germany):

$$R = \left(1 - \frac{C_p}{C_f}\right) \times 100\,\%\,. \quad [9]$$

The flux/permeance recovery ratio was calculated by Eq. **10**:

$$FRR = \frac{J_1}{J_0} \times 100\,\%, \quad [10]$$

where FRR indicates the flux/permeance recovery ratio, and J_0 and J_1 are pure water fluxes before filtration and after membrane regeneration, respectively. In-place cleaning was performed after each-cycle filtration using a dilute H_2O_2 solution (ca. 10 mM, pH 7.5, adjusted by 1 M NaOH) or deionized water.

Computational Simulations. The molecular interactions were calculated by DFT using Gaussian 09 with the GENECP basis set (44, 45). The self-consistent reaction field theory was adopted with water as the solvent. The 3D isosurfaces and corresponding 2D contour maps of the electron density difference of the resulting system were analyzed by Multiwfn 3.7 (46).

Data, Materials, and Software Availability. All study data are included in the article and/or *SI Appendix*.

ACKNOWLEDGMENTS. This work was supported by the National Key R&D Program of China (2023YFE0127000), the National Natural Science Foundation of China (22178076), the Natural Science Foundation of Heilongjiang Province for Distinguished Young Scholars (JQ2020B001), Heilongjiang Touyan Team (HITTY-20190033), and Fundamental Research Funds from the Central Universities of Ministry of Education of China (2023FRFK03047). X.Y. was supported by the China National Postdoctoral Program for Innovative Talents (No. BX2021089), China Postdoctoral Science Foundation (No. 2021M701001), and Heilongjiang Postdoctoral Fund (No. LBH-Z21056). Work at Argonne National Laboratory was supported by the Advanced Materials for Energy-Water Systems Center, an Energy Frontier Research Center funded by Department of Energy, Office of Science, Basic Energy Sciences under contract DE-AC02-06CH11357 (conceptualization and analysis).

Author affiliations: [a]Ministry of Industry and Information Technology Key Laboratory of Critical Materials Technology for New Energy Conversion and Storage, State Key Laboratory of Urban Water Resource and Environment, School of Chemistry and Chemical Engineering, Harbin Institute of Technology, Harbin 150001, People's Republic of China; [b]Longjiang Environmental Protection Group CO., LTD, Harbin 150050, People's Republic of China; [c]School of Marine Science and Technology, State Key Laboratory of Urban Water Resource and Environment, Harbin Institute of Technology, Weihai 264209, People's Republic of China; [d]Institute for Nanotechnology and Water Sustainability, College of Engineering, Science and Technology, University of South Africa, Roodepoort 1709, South Africa; [e]Chemical Sciences and Engineering Division, Argonne National Laboratory, Lemont, IL 60439; [f]Advanced Materials for Energy-Water Systems Energy Frontier Research Center, Argonne National Laboratory, Lemont, IL 60439; and [g]Pritzker School of Molecular Engineering, University of Chicago, Chicago, IL 60637

Author contributions: X.Y., S.B.D., and L.S. designed research; X.Y., Y.L., D.W., L.Y., J.G., Y.W., Y.B., and B.B.M. performed research; X.Y. and L.S. analyzed data; and X.Y., S.B.D., and L.S. wrote the paper.

1. World Health Organization, Drinking water, https://www.who.int/en/news-room/fact-sheets/detail/drinking-water.
2. B. Van der Bruggen, Sustainable implementation of innovative technologies for water purification. *Nat. Rev. Chem.* **5**, 217–218 (2021).
3. S. B. Darling, Perspective: Interfacial materials at the interface of energy and water. *J. Appl. Phys.* **124**, 030901 (2018).
4. J. Eliasson, The rising pressure of global water shortages. *Nature* **517**, 6 (2015).
5. M. A. Shannon *et al.*, Science and technology for water purification in the coming decades. *Nature* **452**, 301–310 (2008).
6. H. B. Park, J. Kamcev, L. M. Robeson, M. Elimelech, B. D. Freeman, Maximizing the right stuff: The trade-off between membrane permeability and selectivity. *Science* **356**, 1138–1148 (2017).

7. L. Chen *et al.*, Ion sieving in graphene oxide membranes via cationic control of interlayer spacing. *Nature* **550**, 380–383 (2017).
8. J. R. Werber, C. O. Osuji, M. Elimelech, Materials for next-generation desalination and water purification membranes. *Nat. Rev. Mater.* **1**, 16018 (2016).
9. S. Karan, Z. Jiang, A. G. Livingston, Sub-10 nm polyamide nanofilms with ultrafast solvent transport for molecular separation. *Science* **348**, 1347–1351 (2015).
10. X. Yang, A. B. Martinson, J. W. Elam, L. Shao, S. B. Darling, Water treatment based on atomically engineered materials: Atomic layer deposition and beyond. *Matter* **4**, 3515–3548 (2021).
11. E. Barry *et al.*, Advanced materials for energy-water systems: The central role of water/solid interfaces in adsorption, reactivity, and transport. *Chem. Rev.* **121**, 9450–9501 (2021).
12. X. Yang *et al.*, Protein-activated atomic layer deposition for robust crude-oil-repellent hierarchical nano-armored membranes. *Sci. Bull.* **69**, 218–226 (2024).
13. R. Zhang *et al.*, Antifouling membranes for sustainable water purification: Strategies and mechanisms. *Chem. Soc. Rev.* **45**, 5888–5924 (2016).
14. Y. Zhao *et al.*, Pulsed hydraulic-pressure-responsive self-cleaning membrane. *Nature* **608**, 69–73 (2022).
15. D. Dong *et al.*, Double defense design of super-anti-fouling membranes for oil/water emulsion separation. *Adv. Funct. Mater.* **32**, 2113247 (2022).
16. W. Yang *et al.*, A universal strategy for constructing robust and antifouling cellulose nanocrystal coating. *Adv. Funct. Mater.* **32**, 2109989 (2022).
17. D. Miller, D. Dreyer, C. Bielawski, D. Paul, B. Freeman, Surface modification of water purification membranes. *Angew. Chem. Int. Ed. Engl.* **129**, 4662–4711 (2016).
18. J. Friedrichs *et al.*, Entropic repulsion of cholesterol-containing layers counteracts bioadhesion. *Nature* **618**, 733–739 (2023).
19. H. Zhang, Y. Wan, J. Luo, S. B. Darling, Drawing on membrane photocatalysis for fouling mitigation. *ACS Appl. Mater. Interfaces* **13**, 14844–14865 (2021).
20. H. Zhang, A. U. Mane, X. Yang, Z. Xia, S. B. Darling, Visible-light-activated photocatalytic films toward self-cleaning membranes. *Adv. Funct. Mater.* **30**, 2002847 (2020).
21. C. Zhang *et al.*, Polydopamine-coated porous substrates as a platform for mineralized β-FeOOH nanorods with photocatalysis under sunlight. *ACS Appl. Mater. Interfaces* **7**, 11567–11574 (2015).
22. A. Xie *et al.*, Graphene oxide/Fe (III)-based metal-organic framework membrane for enhanced water purification based on synergistic separation and photo-Fenton processes. *Appl. Catal. B: Environ.* **264**, 118548 (2020).
23. H. Ejima *et al.*, One-step assembly of coordination complexes for versatile film and particle engineering. *Science* **341**, 154–157 (2013).
24. H. Geng *et al.*, Metal ion-directed functional metal-phenolic materials. *Chem. Rev.* **122**, 11432–11473 (2022).
25. W. Yan, M. Shi, C. Dong, L. Liu, C. Gao, Applications of tannic acid in membrane technologies: A review. *Adv. Colloid Interface Sci.* **284**, 102267 (2020).
26. Z. Wang *et al.*, One-step transformation of highly hydrophobic membranes into superhydrophilic and underwater superoleophobic ones for high-efficiency separation of oil-in-water emulsions. *J. Mater. Chem. A* **6**, 3391–3396 (2018).
27. X. Yang *et al.*, Polyphenol-sensitized atomic layer deposition for membrane interface hydrophilization. *Adv. Funct. Mater.* **30**, 1910062 (2020).
28. L. Q. Xu, K. G. Neoh, E. T. Kang, Natural polyphenols as versatile platforms for material engineering and surface functionalization. *Prog. Polymer Sci.* **87**, 165–196 (2018).
29. T. S. Sileika, D. G. Barrett, R. Zhang, K. H. A. Lau, P. B. Messersmith, Colorless multifunctional coatings inspired by polyphenols found in tea, chocolate, and wine. *Angew. Chem. Int. Ed. Engl.* **52**, 10766–10770 (2013).
30. R. W. Wenzel, Resistance of solid surfaces to wetting by water. *Ind. Eng. Chem.* **28**, 988–994 (1936).
31. J. H. Clint, A. C. Wicks, Adhesion under water: Surface energy considerations. *Int. J. Adhes. Adhes.* **21**, 267–273 (2001).
32. H. Li *et al.*, Bioinspired dynamic antifouling of oil-water separation membrane by bubble-mediated shape morphing. *Adv. Funct. Mater.* **33**, 2212582 (2023).
33. Y. Cai *et al.*, A self-cleaning heterostructured membrane for efficient oil-in-water emulsion separation with stable flux. *Adv. Mater.* **32**, 2001265 (2020).
34. X. Zhao *et al.*, Polyphenol-metal manipulated nanohybridization of CNT membranes with FeOOH nanorods for high-flux, antifouling and self-cleaning oil/water separation. *J. Membr. Sci.* **600**, 117857 (2020).
35. Y. Liu *et al.*, 2D heterostructure membranes with sunlight-driven self-cleaning ability for highly efficient oil-water separation. *Adv. Funct. Mater.* **28**, 1706545 (2018).
36. A. Xie *et al.*, Photo-Fenton self-cleaning membranes with robust flux recovery for an efficient oil/water emulsion separation. *J. Mater. Chem. A* **7**, 8491–8502 (2019).
37. L. Yan *et al.*, Bio-inspired mineral-hydrogel hybrid coating on hydrophobic PVDF membrane boosting oil/water emulsion separation. *Sep. Purif. Technol.* **285**, 120383 (2022).
38. R. Wang *et al.*, Superwetting oil/water separation membrane constructed from in situ assembled metal-phenolic networks and metal-organic frameworks. *ACS Appl. Mater. Interfaces* **12**, 10000–10008 (2020).
39. Y. Zhu *et al.*, Zwitterionic nanohydrogel grafted PVDF membranes with comprehensive antifouling property and superior cycle stability for oil-in-water emulsion separation. *Adv. Funct. Mater.* **28**, 1804121 (2018).
40. H. C. Yang *et al.*, Crude-oil-repellent membranes by atomic layer deposition: Oxide interface engineering. *ACS Nano* **12**, 8678–8685 (2018).
41. L. Zhang, L. Cheng, H. Wu, T. Yoshioka, H. Matsuyama, One-step fabrication of robust and anti-oil-fouling aliphatic polyketone composite membranes for sustainable and efficient filtration of oil-in-water emulsions. *J. Mater. Chem. A* **6**, 24641–24650 (2018).
42. L. Zhang, Y. Lin, L. Cheng, Z. Yang, H. Matsuyama, A comprehensively fouling-and solvent-resistant aliphatic polyketone membrane for high-flux filtration of difficult oil-in-water micro-and nanoemulsions. *J. Membr. Sci.* **582**, 48–58 (2019).
43. R. Wang, X. Zhao, Y. Lan, L. Liu, C. Gao, In situ metal-polyphenol interfacial assembly tailored superwetting PES/SPES/MPN membranes for oil-in-water emulsion separation. *J. Membr. Sci.* **615**, 118566 (2020).
44. M. J. Frisch *et al.*, *Gaussian 09W, Revision A* (Gaussian Inc., Wallingford, CT, 2009).
45. C. Lee, W. Yang, R. G. Parr, Development of the Colle-Salvetti correlation-energy formula into a functional of the electron density. *Phys. Rev. B* **37**, 785 (1988).
46. T. Lu, F. Chen, Multiwfn: A multifunctional wavefunction analyzer. *J. Comput. Chem.* **33**, 580–592 (2012).